

Topography and instability of monolayers near domain boundaries

H. Diamant,¹ T. A. Witten,¹ C. Ege,² A. Gopal,² and K. Y. C. Lee²

¹*James Franck Institute and Department of Physics, University of Chicago,
5640 South Ellis Avenue, Chicago, IL 60637*

²*Department of Chemistry and Institute for Biophysical Dynamics, University of Chicago,
5735 South Ellis Avenue, Chicago, IL 60637*

(February 9, 2001)

We theoretically study the topography of a biphasic surfactant monolayer in the vicinity of domain boundaries. The differing elastic properties of the two phases generally lead to a nonflat topography of “mesas”, where domains of one phase are elevated with respect to the other phase. The mesas are steep but low, having heights of up to 10 nm. As the monolayer is laterally compressed, the mesas develop overhangs and eventually become unstable at a surface tension of about $K(\delta c_0)^2$ (δc_0 being the difference in spontaneous curvature and K a bending modulus). In addition, the boundary is found to undergo a topography-induced rippling instability upon compression, if its line tension is smaller than about $K\delta c_0$. The effect of diffuse boundaries on these features and the topographic behavior near a critical point are also examined. We discuss the relevance of our findings to several experimental observations related to surfactant monolayers: (i) small topographic features recently found near domain boundaries; (ii) folding behavior observed in mixed phospholipid monolayers and model lung surfactants; (iii) roughening of domain boundaries seen under lateral compression; (iv) the absence of biphasic structures in tensionless surfactant films.

68.18.-g,82.70.Uv,87.68.+z

I. INTRODUCTION

Monolayers of amphiphilic molecules (surfactants) at water/air or water/oil interfaces are used in numerous applications to reduce interfacial tension, control wetting properties, stabilize emulsions and foams, *etc.* [1,2]. Monolayers of biological surfactants (phospholipids) are commonly studied as models for the surfaces of cell membranes and are also encountered in various biological systems [3]. An important example is the lung surfactant monolayer covering the alveoli in lungs, whose main function is to lower the surface tension of the lungs, thereby drastically reducing the mechanical work required for breathing [4].

Amphiphilic monolayers generally have a finite spontaneous curvature arising from the asymmetry of the molecules as well as the asymmetry with respect to electrostatic interactions (*i.e.*, the differing dielectric properties of the polar and nonpolar phases forming the interface) [5]. Despite this tendency to bend, homogeneous monolayers are almost always flattened by the water/air or water/oil interfacial tension. Only for very low (sometimes even negative [6]) tension does a nonflat conformation become energetically favorable for a homogeneous monolayer. (This is achieved, *e.g.*, by extensive lateral compression.) Such a reversible departure from a flat, two-dimensional state to a three-dimensional conformation is referred to as the *buckling transition* and has drawn considerable attention [6–8]. However, it is not commonly observed in practice [7], since it is usually preceded by other modes of collapse such as monolayer breakage into multilayers [9,10] and ejection of vesicles or micelles [11]. The possibility to explore the third dimension upon compression is of particular interest in the case of lung surfactant monolayers, which are required to change their projected area significantly during the compression-expansion cycle of breathing.

The two-dimensional fluid comprising a monolayer may separate into domains of different coexisting phases. Single-component monolayers exhibit gas/liquid-expanded, liquid-expanded/liquid-condensed and liquid-condensed/solid coexistence [1–3], whereas mixed monolayers may form domains of differing composition. A special, well-studied property of surfactant monolayers is the stabilization of finite domains and modulated phases due to long-range electrostatic interactions [12,13]. The coupling between lateral variations in composition and curvature was thoroughly studied as well [8,14–20], mainly with regard to various domain structures on surfaces and shape transformations of bilayer vesicles.

Despite extensive research on surfactant monolayers there are important features, in particular of biphasic monolayers, which are not well understood. Recent experiments on mixed phospholipid monolayers have revealed a new type of local folding upon compression, which is believed to be important for the function of lungs [21] (see Fig. 8). Another observed feature is the appearance of rough domain boundaries upon compression [22] (see Fig. 9).

In the current work we study the relation between lateral domain structure and monolayer topography in more detail, focusing on the conformation of monolayers in the vicinity of domain boundaries [23]. We thereby try to

shed some light on the unexplained features mentioned above. Domains of different density and/or composition in a biphasic monolayer should generally have differing elastic properties. The requirements of mechanical equilibrium and smoothness of the monolayer surface lead to nonflat conformations attempting to “reconcile” the different properties of the contiguous domains. These simple mechanical considerations result in a surprisingly rich behavior, including the formation of overhangs and emergence of instabilities, as discussed in the following sections.

The Monge representation and linearization of profile equations have been ubiquitously used in the theoretical modeling of monolayers and membranes [2]. These mathematical simplifications describe the topography by a single-valued height function assumed to have moderate slopes. By contrast, the phenomena discussed in the current work involve, in an essential way, steep slopes and overhangs. We thus avoid the Monge representation and solve the nonlinear profile equations. In order for the mathematics to remain tractable we resort to another simplification—the profile is assumed to be uniform along one lateral direction (namely, the direction parallel to the domain boundary)—rendering the nonlinear equations one-dimensional. This constraint is further discussed in the next section; it is partially relaxed in the treatment of boundary rippling in Sec. V.

The basic model and its assumptions are presented in Sec. II. We then proceed in Sec. III to review the simplest case of an infinitely sharp, straight domain boundary [23]. Despite its simplicity, this limiting case demonstrates most of our qualitative results. The calculation is refined in Sec. IV where a boundary of nonzero thickness is considered. In Sec. V we study the stability of a straight domain boundary to lateral undulations. The topographic behavior of a monolayer near its critical point is examined in Sec. VI. Finally, in Sec. VII, we discuss the various results and their relevance to experiments.

II. THE MODEL

Four length scales are distinguished when studying the elasticity of a biphasic monolayer: the typical domain size, L , the width of a domain boundary, ξ , the typical spontaneous radius of curvature, c_0^{-1} , and the elastic length, $\lambda = (K/\gamma)^{1/2}$, determining the lateral extent of height variations (K being the bending modulus and γ the surface tension). An important observation is that in most practical cases the domain size is much larger than all other length scales— L is typically of order 10 μm , whereas ξ , c_0^{-1} and λ are of order 1–10 nm. This allows us to focus on a single, straight boundary between two large domains and regard the centers of the domains as infinitely far away. We thus represent the boundary region as a surface whose far left and far right have different spontaneous curvatures, c_{01} and c_{02} [24]. (Throughout this paper we assume, without loss of generality, $c_{01} > c_{02}$.) The surface is uniform in the y direction parallel to the boundary but can curve in the perpendicular x direction, as depicted in Fig. 1A.

In fact, an inflected conformation perpendicular to the boundary is a straightforward consequence of such a lateral structure. Far away from the boundary (*i.e.*, at the centers of the two contiguous domains) the surface is flat. Because of the nonzero spontaneous curvature the far left side is subjected to a bending moment of Kc_{01} , supplemented by a tensile torque of $-\gamma h_1$, where $-h_1$ is the height of this side relative to the boundary (see Fig. 1B). Similarly, a moment of $Kc_{02} + \gamma h_2$ is exerted on the far right side. Mechanical equilibrium requires that these two moments balance each other, *i.e.*,

$$h = h_1 + h_2 = K\delta c_0/\gamma = \lambda^2\delta c_0, \quad (1)$$

where $\delta c_0 \equiv c_{01} - c_{02}$. Thus, an inflected conformation with a finite height difference occurs for any finite δc_0 and γ . A measure of the inflection sharpness is $h/\lambda = \lambda\delta c_0$. As compression increases (*i.e.*, γ decreases [25]), the inflection becomes higher and sharper. Note that the integrated height difference is insensitive to details of the inner boundary region. Equation (1) can therefore serve as a rigorous sum rule for more detailed calculations such as those presented in Secs. III and IV.

The elastic energy to be minimized in order to find the monolayer topography [26] is

$$G = \int_A dA \left(\frac{1}{2} K c^2 - K c_0 c \right) + \gamma \int_A d(A - A_p) + \tau \int_{\mathbf{R}} d(R - y), \quad (2)$$

where A denotes the monolayer surface, A_p its projection onto the xy reference plane, c the local surface curvature, \mathbf{R} the trajectory of the domain boundary, and τ the line tension of the boundary. The functional (2) has been defined such that a flat surface with a straight domain boundary running parallel to the y axis is the reference state of zero energy. Since the surface we consider in Secs. III and IV is uniform in the y direction, we may represent it by the local angle $\theta(s)$ it makes with the reference xy plane at curvilinear distance s from the boundary (see Fig. 1B). The energy functional (2) is then rewritten as

$$g[\theta(s)] \equiv \frac{G}{L} = \int_{-\infty}^{\infty} ds \left[\frac{1}{2} K \dot{\theta}^2 - K c_0 \dot{\theta} + \gamma(1 - \cos \theta) \right], \quad (3)$$

where L is the length of the boundary, a dot denotes d/ds , and c_0 is not regarded as a constant but varies with s . In order for the surface to be smooth everywhere we require that $\theta(s)$ be a continuous function [27]. It is useful to notice that, despite the linear term in $\dot{\theta}$, the functional (3) is invariant under s -reversal, $s \rightarrow -s$. This is because we can break any plausible choice of $c_0(s)$ into a constant, $(c_{01} + c_{02})/2$, plus an odd function of s and, assuming that the surface becomes flat far away from the boundary, the constant term does not contribute to the integral. In other words, we may specialize to the case $c_{01} = -c_{02}$. Hence, minimization will necessarily produce symmetric angle profiles $\theta(s)$ and antisymmetric topographies $h(s)$. (Note that this argument does not hold if K is taken as nonuniform [23].)

III. SHARP DOMAIN BOUNDARY

We begin with the simple case where the boundary thickness ξ is much smaller than the other length scales, extending our earlier work [23]. (We show in Sec. IV that the condition for this sharp limit is in fact weaker, the requirement being merely $\xi \delta c_0 \ll 1$.) In this limit the boundary may be regarded as infinitely sharp, accompanied by a step-function jump in spontaneous curvature,

$$c_0 = \begin{cases} c_{01} & s < 0 \\ c_{02} & s > 0. \end{cases}$$

Substituting this spatial variation of c_0 in Eq. (3) we can integrate the linear term in $\dot{\theta}$. The energy is then rewritten as

$$g[\theta(s)] = \int_{-\infty}^{\infty} ds \left[\frac{1}{2} K \dot{\theta}^2 + \gamma(1 - \cos \theta) \right] - K \delta c_0 \theta_0, \quad (4)$$

where $\theta_0 \equiv \theta(s=0)$ is the maximum inflection angle.

The integral in Eq. (4) has the familiar form of the Sine-Gordon action. Variation with respect to $\theta(s \neq 0)$ gives a Sine-Gordon profile equation,

$$\ddot{\theta} = \lambda^{-2} \sin \theta. \quad (5)$$

First integration of Eq. (5) yields

$$\dot{\theta} = \begin{cases} 2\lambda^{-1} \sin(\theta/2) & s < 0 \\ -2\lambda^{-1} \sin(\theta/2) & s > 0. \end{cases} \quad (6)$$

In the current, simple case, due to the boundary conditions $\theta(s \rightarrow \pm\infty) = 0$, second integration can be carried out as well. The following soliton profile is obtained:

$$\tan \frac{\theta}{4} = \tan \frac{\theta_0}{4} \exp(-|s|/\lambda). \quad (7)$$

Finally, we need a condition for the jump in curvature at the sharp boundary. This is derived mathematically by either integrating $\dot{\theta}$ of Eq. (5) over an infinitesimal length around the boundary, or taking the variation of g with respect to θ_0 . The same result is obtained, nonetheless, by a simple moment-balance argument: the bending moment acting on the boundary from the left, $K[\dot{\theta}(0^-) - c_{01}]$, must balance the one acting from the right, $K[\dot{\theta}(0^+) - c_{02}]$. Hence,

$$\dot{\theta}(0^-) - \dot{\theta}(0^+) = \delta c_0,$$

which determines θ_0 as

$$\sin \frac{\theta_0}{2} = \frac{\lambda \delta c_0}{4} = \frac{h}{4\lambda}. \quad (8)$$

The dependence of the slope on the ratio h/λ in the sharp-boundary limit readily follows from dimensional analysis. Yet, the exact nonlinear dependence given by Eq. (8) is essential for our main results, as will be demonstrated below.

Thus, we infer again that for any finite δc_0 and γ the monolayer attains an inflected shape whose profile is given by Eqs. (7) and (8). Integrating $\int_{-\infty}^{\infty} ds \sin \theta(s)$, one verifies that the general sum rule for the total height difference, Eq. (1), is satisfied. The energy of the inflected conformation is calculated by substituting the obtained profile back in Eq. (4),

$$g(\theta_0) = K \delta c_0 \left(2 \tan \frac{\theta_0}{4} - \theta_0 \right), \quad (9)$$

which, as expected, is negative for $\theta_0 < \pi$, *i.e.*, the inflected shape is favored over the flat one. We also calculate the projected area as a function of tension, either by integration, $A_p = L \int_{-\infty}^{\infty} ds \cos \theta$, or by the following derivative,

$$\Delta L \equiv \frac{A - A_p}{L} = \frac{\partial g}{\partial \gamma} = \frac{32}{\delta c_0} \sin \frac{\theta_0}{2} \sin^2 \frac{\theta_0}{4}, \quad (10)$$

and the lateral compressibility,

$$C = -\frac{\partial \Delta L}{\partial \gamma} = \frac{1}{K(\delta c_0)^3} \frac{[4 \sin(\theta_0/2)]^3 \sin(3\theta_0/2)}{\cos(\theta_0/2)}. \quad (11)$$

As the monolayer is compressed by progressively decreasing γ or increasing ΔL (depending on the experimental setup), the inflected profile becomes sharper (larger θ_0 , Eq. (8)), higher (larger h , Eq. (1)) and more favorable (lower g , Eq. (9)). The process is demonstrated in Fig. 2. For $\gamma < \frac{1}{8}K(\delta c_0)^2$ the inflection angle θ_0 becomes larger than $\pi/2$ and a stable overhang forms. However, beyond a critical value of compression,

$$\gamma < \gamma_c = \frac{1}{16}K(\delta c_0)^2, \quad \Delta L > \Delta L_c = \frac{16}{\delta c_0}, \quad (12)$$

Eq. (8) has no solution. This occurs in the current calculation when $\theta_0 = \theta_{0c} = \pi$, at which point the inflection remains finite, $h = h_c = 16/\delta c_0$, yet the lateral compressibility diverges,

$$C \sim (\pi - \theta_0)^{-1} \sim (\gamma - \gamma_c)^{-1/2}. \quad (13)$$

Note that this instability is revealed only in the nonlinear representation of the elastic problem (*e.g.*, *via* Eq. (8) which is nonlinear in θ_0). A theory relying on the Monge representation and moderate slopes would inevitably miss it.

The divergence of lateral compressibility implies that extra surface area can be pulled into the boundary region without resistance. Thus, one expects the monolayer to attain a folded structure that will be stabilized by higher, nonlinear-elastic terms. A detailed description of this folded shape is beyond the scope of the current work. Moreover, the transition from an inflected to a folded state is treated here as a spinodal-like instability. A more detailed study might yield a folded structure as energetically favorable prior to this instability, *i.e.*, a binodal-like transition preceding the one treated here. In a macroscopic measurement of a pressure–area isotherm the instability will appear as a plateau, much like any other 1st-order transition. Hence, distinguishing it from other mechanisms requires microscopic visualization of the monolayer [28].

IV. DIFFUSE DOMAIN BOUNDARY

We now examine the effect of a domain boundary of finite thickness. That is, we suppose that rather than changing abruptly, c_0 varies gradually from c_{01} to c_{02} over a distance ξ . We begin with a heuristic argument for the limit of a very diffuse boundary, where ξ is much larger than λ and $(\delta c_0)^{-1}$. Consider a small element ds in the boundary region. The difference in bending moments acting on its two ends, $Kd(\dot{\theta} - c_0) = K(\ddot{\theta} - \dot{c}_0)ds$, is balanced by a difference in tensile torque $\gamma dh = \gamma \sin \theta ds$. In the limit of very large ξ the curvature changes very slowly, such that $\ddot{\theta} \sim \theta_0/\xi^2$ is negligible compared to $\dot{c}_0 \sim -\delta c_0/\xi$. We thus obtain

$$\sin \theta_0 \sim \lambda^2 \delta c_0 / \xi = h / \xi. \quad (14)$$

The mesa slope in this diffuse limit, unsurprisingly, depends on h/ξ rather than h/λ . We can infer from Eq. (14) several less expected results as well. The equation has no solution for $\theta_0 > \theta_{0c} = \pi/2$ (rather than π), whereupon the mesa height is of the order of ξ , *i.e.*, very large compared to λ . Thus, at the critical compression the entire wide boundary lies almost vertically, having a small lateral dimension. The critical tension is

$$\gamma_c \sim K\delta c_0/\xi, \quad (15)$$

i.e., much smaller than its value in the sharp limit ($\sim K(\delta c_0)^2$), implying that the monolayer can sustain much higher compression than in the sharp case. (Naturally, as ξ tends to infinity one expects the resulting almost-uniform monolayer to become increasingly stable to the heterogeneity-driven folding.)

In order to check these results in more detail and study the crossover between the sharp and diffuse limits, we now turn to a detailed treatment of a simple, specific example. Let us assume that the spontaneous curvature c_0 changes linearly across the boundary,

$$c_0 = \begin{cases} c_{01} & s < -\xi/2 \\ c_{01} - \delta c_0(s/\xi + 1/2) & -\xi/2 < s < \xi/2 \\ c_{02} & s > \xi/2. \end{cases}$$

Substituting the spatial dependence of c_0 in the energy functional (3) and taking the variation with respect to $\theta(s)$, we obtain the following profile equations:

$$\ddot{\theta} = \begin{cases} \lambda^{-2} \sin \theta & |s| > \xi/2 \\ \lambda^{-2} \sin \theta - \delta c_0/\xi & |s| < \xi/2. \end{cases} \quad (16)$$

The boundary conditions in the current case are continuity of θ and $\dot{\theta}$ at $s = \pm\xi/2$ and, as before, flatness at infinity.

First integration of Eq. (16) gives

$$\dot{\theta}^2 = \begin{cases} 4\lambda^{-2} \sin^2 \frac{\theta}{2} & |s| > \xi/2 \\ 4\lambda^{-2} \sin^2 \frac{\theta}{2} - (2\delta c_0/\xi)(\theta - \theta_1) & |s| < \xi/2, \end{cases} \quad (17)$$

where $\theta_1 \equiv \theta(-\xi/2) = \theta(\xi/2)$. As in Sec. III, we can now calculate the energy of the inflected conformation as a function of θ_0 and θ_1 by substituting the profile (17) back in the energy functional (3). The result is

$$\frac{g(\theta_0, \theta_1)}{K\delta c_0} = \frac{4}{\lambda\delta c_0} \left\{ 4 \sin^2 \frac{\theta_1}{4} + \int_{\theta_1}^{\theta_0} d\theta \left[\sin^2 \frac{\theta}{2} - \frac{\lambda^2 \delta c_0}{2\xi} (\theta - \theta_1) \right]^{1/2} \right\} - \theta_1. \quad (18)$$

Second integration, which would yield the topographic profile, cannot be analytically performed in the current case. Instead, we seek the equation for θ_0 which replaces Eq. (8) for finding the point of instability. Minimizing g of Eq. (18) with respect to θ_0 gives one relation between θ_0 and θ_1 ,

$$\theta_0 - \theta_1 = \frac{2\xi}{\lambda^2 \delta c_0} \sin^2 \frac{\theta_0}{2}. \quad (19)$$

This equation reflects a moment balance for the section $-\infty < s < 0$; it is also obtained by setting $\dot{\theta}(0) = 0$ in Eq. (17). Minimization with respect to θ_1 yields the second relation between θ_0 and θ_1 ,

$$\int_{\theta_1}^{\theta_0} \left[\frac{2\xi}{\lambda^2 \delta c_0} \sin^2 \frac{\theta}{2} - (\theta - \theta_1) \right]^{-1/2} d\theta = \left(\frac{\xi \delta c_0}{2} \right)^{1/2}. \quad (20)$$

It stems from the moment balance on the section $-\xi/2 < s < 0$ and can be also obtained from integration of the profile equation (16) along this section.

Equations (19) and (20) can be solved numerically for θ_0 . As in Sec. III, one finds a minimum value $\gamma = \gamma_c$ (*i.e.*, a maximum value of λ) beyond which there is no solution to the equations and the monolayer becomes unstable. From the fact that the various parameters are grouped in Eqs. (19) and (20) into two dimensionless terms, $\xi\delta c_0$ and $\xi/(\lambda^2\delta c_0) = \xi/h$, it follows that the critical tension must satisfy the scaling law

$$\gamma_c = \frac{K\delta c_0}{\xi} F(\xi\delta c_0) \quad (21)$$

where $F(x)$ is a certain ‘‘universal’’, dimensionless function. In Fig. 3A we have plotted the function $F(x)$ as obtained from numerical integration of Eqs. (19) and (20).

In the sharp limit, $\xi\delta c_0 \ll 1$, γ_c must become independent of ξ . Hence, $F(x)$ is linear for small x so as to get $\gamma_c \sim K(\delta c_0)^2$. Indeed, in this limit Eq. (20) reduces to $\theta_0 - \theta_1 \simeq \xi\delta c_0/8$ which, together with Eq. (19), recovers

the results of Sec. III (cf. Eqs. (8) and (12)), $\sin(\theta_0/2) \simeq \lambda\delta c_0/4 = h/(4\lambda)$, $\theta_{0c} \simeq \pi$, and $\gamma_c \simeq \frac{1}{16}K(\delta c_0)^2$. We thus conclude that the results of Sec. III are valid as long as $\xi \ll (\delta c_0)^{-1}$.

In the diffuse limit, $\xi\delta c_0 \gg 1$, Eq. (20) reduces to

$$\sin \theta_0 \simeq \lambda^2\delta c_0/\xi = h/\xi, \quad (22)$$

as was anticipated in Eq. (14). This leads to $\theta_{0c} \simeq \pi/2$, $\gamma_c \simeq K\delta c_0/\xi$. Hence $F(x) \simeq 1$ for $x \gg 1$, as is verified in Fig. 3A.

To summarize these results:

$$\begin{aligned} \gamma_c &= \frac{K\delta c_0}{\xi} F(\xi\delta c_0) \\ F(x) &\simeq \begin{cases} x/16 & x \ll 1 \\ 1 & x \gg 1. \end{cases} \end{aligned} \quad (23)$$

Recall that we have obtained the results in both the sharp and diffuse limits independently of the detailed shape of $c_0(s)$. Hence, varying the spatial dependence of c_0 would merely affect the exact shape of $F(x)$ in between these limits. The more diffuse the boundary, the higher the compression required for folding, the higher the mesa wall at the instability, and the smaller the critical inflection angle. Diffuse boundaries thus allow a biphasic monolayer to withstand stronger compression and higher mesas. Despite the smaller inflection angle there is always an overhang topography at the instability, *i.e.*, $\pi/2 < \theta_{0c} < \pi$. The dependence of the critical inflection angle on boundary thickness is shown in Fig. 3B.

V. INSTABILITY OF THE DOMAIN BOUNDARY

Until now we have considered only topographies which do not vary along the direction of the domain boundary, and thus do not affect its length. The departure from a flat conformation near a domain boundary, as studied in the previous sections, is energetically beneficial, *i.e.*, the inflection energy per unit length, g , is negative. Hence, as far as the topographic effect is concerned, it would be favorable to increase the boundary length. In other words, the topography effectively reduces the line tension of the phase boundary, the reduction being given by g of Eqs. (9) or (18) for a sharp or diffuse boundary, respectively. Consequently, if the bare line tension of the boundary [29], τ , is smaller than the maximum value of $|g|$, then, for a certain inflection angle $\theta_0 < \theta_{0c}$, the effective line tension will turn negative and one expects the boundary to ripple. Assuming hereafter a sharp boundary, we obtain the condition for rippling by setting $\theta_0 = \theta_{0c} = \pi$ in Eq. (9) [30],

$$\tau < \tau_c = (\pi - 2)K\delta c_0. \quad (24)$$

The inflection angle and surface tension required for rippling, θ_{0r} and γ_r , are then obtained from the equations

$$\begin{aligned} \theta_{0r} - 2 \tan \frac{\theta_{0r}}{4} &= \frac{\tau}{K\delta c_0} \\ \gamma_r &= \frac{\gamma_c}{\sin^2(\theta_{0r}/2)}, \end{aligned} \quad (25)$$

where, as defined in Eq. (12), $\gamma_c = \frac{1}{16}K(\delta c_0)^2$. The diagram in Fig. 4 summarizes the results concerning the topographic transitions near a sharp boundary as a function of surface tension and line tension.

Let us now examine the spatial form of the rippling transition. In Sec. III we assumed a straight, sharp domain boundary, which can be represented in Cartesian coordinates as the line $\mathbf{R}(y) = (x = 0, y, z = 0)$. We now wish to perturb the inflected conformation by considering a boundary that slightly wiggles with amplitude a and wave number q . The full three-dimensional problem is formidable. We therefore restrict ourselves to a simple subset of perturbations—uniform displacements of the inflected shape in the x direction, whose magnitude undulates in the y direction (see Fig. 5). Since we do not exhaust all available conformations, the minimum energy that we are about to calculate might be higher than the true minimum. Hence, the following results should be considered as an upper-bound estimate for the rippling instability. Nevertheless, this estimate is expected to be good as long as the wiggling wavelength is much larger than the inflection extent, $q\lambda \ll 1$. In this limit the two lateral length scales can be separated, as has been done in Sec. III, and one expects the preferred perturbations to resemble that of Fig. 5. Employing this simplification, we can represent the perturbed boundary by the curve $\mathbf{R}(y) = (x = a \sin qy, y, z = 0)$, and conveniently parameterize the monolayer surface as

$$\begin{aligned}\mathbf{r}(s, t) &= (x(s, t), y(s, t), z(s, t)) \\ x(s, t) &= \int_0^s \cos \theta(s') ds' + a \sin qt, \quad y(s, t) = t, \quad z(s, t) = \int_0^s \sin \theta(s') ds',\end{aligned}$$

such that in the “material coordinates” (s, t) the boundary line is again given by $\mathbf{R}(t) = (s = 0, t, z = 0)$.

In order to use the energy functional (2) we need to represent the geometrical parameters of the surface—its mean curvature $c(s, t)$, area element $dA(s, t)$, projected area element $dA_p(s, t)$, and boundary arc-length $dR(s, t)$ —using the new coordinates. This technical calculation is presented in the Appendix.

Substituting Eqs. (A3)–(A6) into the elastic energy expression, Eq. (2), and expanding to second order in the rippling amplitude a , we obtain

$$\begin{aligned}g[\theta(s)] &\equiv G/L = g^{(0)} + a^2 g^{(1)} \\ g^{(1)} &= \frac{1}{4} (\tau' q^2 + b q^4),\end{aligned}\tag{26}$$

where $g^{(0)}[\theta(s)]$ is the energy functional in the straight case, given by Eq. (3), and $L = \int dt$. The coefficients τ' and b are functionals of the topography $\theta(s)$:

$$\begin{aligned}\tau' &= \tau + \int ds \left[K \left(2 - \frac{5}{2} \sin^2 \theta \right) \dot{\theta}^2 - 2Kc_0 \cos^2 \theta \dot{\theta} + \gamma \sin^2 \theta \right] \\ b &= K \int ds \sin^2 \theta.\end{aligned}\tag{27}$$

They act as effective line tension and bending modulus, respectively. The one-dimensional bending modulus b is proportional to K , the two-dimensional modulus of the sheet; when the boundary curves the monolayer must bend with it (see Fig. 5), leading to a cost in bending energy.

In principle one could now minimize g of Eq. (26) with respect to $\theta(s)$ and find the perturbed shape, $\theta(s) = \theta^{(0)}(s) + a^2 \theta^{(1)}(s)$. However, since $\delta g^{(0)}/\delta \theta^{(0)} = 0$, substituting the perturbed shape back in g would yield, up to order a^2 , $g = g^{(0)}[\theta^{(0)}] + a^2 g^{(1)}[\theta^{(0)}]$. Thus, if we are merely interested in the perturbed *energy*, we may just substitute in Eq. (27) the unperturbed topography $\theta^{(0)}(s)$ as found in Sec. III (Eqs. (6) and (8)). This yields

$$\begin{aligned}\tau' &= \tau - K \delta c_0 \left(\theta_0 - 2 \tan \frac{\theta_0}{4} \right) \\ b &= \frac{32K}{3\delta c_0} \sin \frac{\theta_0}{2} \left(1 - \cos^3 \frac{\theta_0}{2} \right).\end{aligned}\tag{28}$$

When the effective line tension vanishes, $\tau' = 0$, there is a $q = 0$ (*i.e.*, 2nd-order) rippling transition, as already anticipated in Eqs. (24) and (25). (Strictly speaking, since the domain boundary is finite and closed, the transition is encountered only at $\tau' = -\pi^2 b/L^2$, *i.e.*, for the lowest-order undulation of $q = \pi/L$.) The rippling of the one-dimensional boundary is thus analogous to the Euler buckling of an elastic rod [31].

Upon further compression, or if the monolayer is “quenched” to $\tau' < 0$, all modes satisfying

$$q < q^* = \left(\frac{-\tau'}{b} \right)^{1/2} = \frac{\sqrt{3}}{4\sqrt{2}} \delta c_0 \left[\frac{\theta_0 - 2 \tan(\theta_0/4) - \tau/(K\delta c_0)}{\sin(\theta_0/2)[1 - \cos^3(\theta_0/2)]} \right]^{1/2},\tag{29}$$

become unstable and their amplitudes start growing. We expect the observed unstable modes to have roughly the same scale as the upper bound q^* . The scale of the rippling wavelength is thus set by $(\delta c_0)^{-1}$, which is usually much smaller than the boundary length L . Hence, although this is strictly a $q = 0$ instability, one expects in practice to observe a densely wiggling boundary on the scale of the entire domain. Another interesting observation is that, beyond the onset of rippling, q^* does not always increase monotonically with compression. The nonmonotonic behavior becomes more pronounced the smaller the value of $\tau/(K\delta c_0)$, as demonstrated in Fig. 6. For small values of this parameter, therefore, one expects the boundary to ripple densely beyond the onset of instability and then, upon further compression, return to a less rough shape. Recall that our Ansatz concerning the preferred perturbation is expected to give reliable results as long as $q \ll \lambda^{-1}$. We have found that the rippling modes obey $q \lesssim \delta c_0$. On the other hand, a stable, sharp topography requires $\lambda^{-1} \gtrsim \delta c_0/4$ (see Eq. (8)). Thus, our assumption is only marginally fulfilled and the results should be regarded merely as a qualitative guide.

VI. BEHAVIOR NEAR A CRITICAL POINT

The topographic effects described in this article rely on a contrast between different domains. Hence, when a monolayer at coexistence reaches a critical point, these effects are expected to vanish along with the domain structure. Various parameters affecting the topography dramatically change when the critical point is approached: the density contrast becomes increasingly weak (leading to a smaller δc_0), domain boundaries get diffuse (larger ξ), and the bare line tension between domains, τ , tends to zero. Thus, although the topography must clearly disappear at the critical point, its exact behavior has to be examined in detail. For example, it is unclear *a priori* whether, with respect to topography, the monolayer is driven towards the diffuse limit (larger $\xi\delta c_0$) or the sharp one (smaller $\xi\delta c_0$).

As the temperature T approaches its critical value T_c , $\hat{T} \equiv |T - T_c|/T_c \rightarrow 0$, we have [32]

$$\begin{aligned}\xi &\sim \hat{T}^{-\nu} \rightarrow \infty \\ \delta c_0 &\sim \hat{T}^{\beta} \rightarrow 0,\end{aligned}\tag{30}$$

where, for a two-dimensional fluid, $\nu = 1$ and $\beta = 1/8$. Hence, the height difference, given by Eq. (1), decays as

$$h = \lambda^2 \delta c_0 \sim \hat{T}^{\beta} = \hat{T}^{1/8}.\tag{31}$$

Since $\xi\delta c_0 \sim \hat{T}^{-\nu+\beta} \sim \hat{T}^{-7/8} \rightarrow \infty$, it is the diffuse limit of Sec. IV that applies near the critical point. (The three-dimensional topography could affect the critical behavior of the two-dimensional fluid in the monolayer as a “hidden”, annealed variable. Hence, the critical exponents should be modified according to the Fisher renormalization [33]. In the case of a two-dimensional fluid (or Ising model), however, the Fisher renormalization leaves the exponents intact.)

We now explore further details of the topographic critical behavior. For small inflection angles we expect in the diffuse limit (cf. Eq. (22))

$$\theta_0 \simeq h/\xi \sim t^{\nu+\beta} = \hat{T}^{9/8}.\tag{32}$$

Indeed, the topography has been found in Sec. IV to depend on two dimensionless quantities, $\xi\delta c_0$ and $\xi/(\lambda^2\delta c_0) = \xi/h$, both of which diverge at the critical point—the former as $\hat{T}^{-\nu+\beta} = \hat{T}^{-7/8}$ and the latter as $\hat{T}^{-\nu-\beta} = \hat{T}^{-9/8}$. Studying Eqs. (19) and (20) in this asymptotic limit, one finds $\theta_0 \simeq h/\xi$ and $\theta_1 \simeq \theta_0/2$, which verifies Eq. (32). Substituting these results in Eq. (18) for the inflection energy, we get

$$g \simeq -\frac{K\lambda^2\delta c_0^2}{2\xi} \sim \hat{T}^{\nu+2\beta} = \hat{T}^{5/4}.\tag{33}$$

Thus, the topographic contribution to the heat capacity of the monolayer vanishes as $\partial g/\partial \hat{T} \sim \hat{T}^{1/4}$, whereas the heat capacity of the two-dimensional fluid diverges logarithmically [32]. This consistently demonstrates that the critical behavior of the monolayer remains unaffected by the topography.

How does the approach to the critical point influence the instabilities studied in the previous sections? The folding instability in the diffuse limit requires, according to Eq. (23), a surface tension lower than

$$\gamma_c \simeq K\delta c_0/\xi \sim \hat{T}^{\nu+\beta} \sim \hat{T}^{9/8} \rightarrow 0.\tag{34}$$

In practice, therefore, as soon as the required lateral pressure exceeds that of the critical point the folding instability will become unattainable.

The effect on the boundary-rippling instability studied in Sec. V is more delicate. Upon approaching the critical point the bare line tension of the boundary gets vanishingly small as [34,35]

$$\tau \sim \hat{T}^{\mu} \rightarrow 0, \quad \mu = 1.\tag{35}$$

Thus, the resistance to rippling becomes increasingly weak. Yet, at the same time the driving force for rippling, *i.e.*, the energy g gained due to the inflected topography, gets weaker as well. According to Eq. (33) the latter vanishes slightly faster, as $\hat{T}^{5/4}$. Hence, it is the bare line tension that wins close to the critical point, and the boundary topography should flatten out at T_c as a smooth step without ripples.

VII. DISCUSSION

We have demonstrated in this work that biphasic monolayers are generally nonflat, having inflected shapes in the vicinity of domain boundaries. This leads to an overall topography of mesas where domains of one phase are higher than those of the other. As the monolayer is progressively compressed the mesas grow more pronounced, subsequently developing overhangs, and finally becoming unstable.

Substituting typical values for phospholipid monolayers [2]— $\gamma \simeq 10\text{--}50$ erg/cm², $K \simeq 10\text{--}50$ $k_B T$, $c_0^{-1} \simeq 5\text{--}10$ nm—we get $\lambda \simeq 1\text{--}10$ nm, $\lambda\delta c_0 \simeq 0.1\text{--}1$, and $h \simeq 0.1\text{--}10$ nm. Hence, the mesas are steep but low. The numerical value of $\lambda\delta c_0$ implies that the predicted instability ($\lambda\delta c_0 \geq 4$) may be observed for attainable pressures. The energy per unit length gained by departing from the flat state to a sharp inflection is, according to Eq. (9), $g \simeq K\delta c_0 \simeq 1\text{--}10$ $k_B T$ /nm. Hence, for a typical domain size of $L \sim 1\text{--}10$ μm , the inflected conformation is “frozen”, *i.e.*, robust under thermal fluctuations. This justifies our mechanical, “zero-temperature” approach.

As a more specific example, we may consider a monolayer whose behavior is governed by electrostatic interactions. The deviation from a flat conformation is thereby driven by variations in the lateral charge density, $\sigma(s)$. In the typical case of strong screening, $c/\kappa \ll 1$, where κ^{-1} is the Debye screening length, one obtains [5] $Kc_0 = \pi\sigma^2/\epsilon\kappa^2$ and $K = 3\pi\sigma^2/2\epsilon\kappa^3$, ϵ being the dielectric constant of water. (Note the finite, positive c_0 ; charged monolayers spontaneously tend to curve into the aqueous phase.) Consequently, substituting typical values of $\sigma \simeq 1$ charge per $0.3\text{--}1$ nm² and $\kappa^{-1} \simeq 1\text{--}10$ nm, we reach similar conclusions to those above.

We have studied domain boundaries of finite thickness as well. The qualitative features of inflected conformation and instability do not disappear for any boundary thickness ξ . On one hand, for a given compression a diffuse boundary leads to more moderate slopes compared to a sharp one. On the other hand, it shifts the folding instability to a higher pressure, thus strengthening the monolayer and allowing for higher mesas to be stabilized. Unfortunately, conventional means of increasing ξ , *e.g.*, heating towards a critical point, also reduce the domain contrast δc_0 , thus suppressing the topography. We have studied this delicate interplay close to a critical point in Sec. VI. Our results for diffuse boundaries show that the simple, infinitely sharp limit gives good results as long as $\xi < (\delta c_0)^{-1}$, which holds in most practical circumstances except near a critical point.

One might worry about additional factors that would destroy the inferred topography. Such a factor is the cost in gravitational energy of displacing water from the flat interface. This energy per unit area is about $\delta\rho gh^2 \sim 10^4$ $k_B T$ /cm², where $\delta\rho$ is the difference in density of the two phases and g is here the gravitational acceleration. Thus, due to the small height of the mesas (1–10 nm), gravity is negligible over all relevant lateral length scales (up to meters). (Beyond the topographic instability, however, the monolayer may become much more folded, and gravity may have a significant stabilizing role.) Another factor to worry about is the van der Waals attraction between the inferred overhang and the underlying surface, which might make the overhang collapse. The attraction energy per unit area is roughly H/h^2 , where H is the Hamaker constant divided by 12π (typically a few $k_B T$) and $h \simeq \lambda^2\delta c_0$ is the overhang height [36]. The lateral extent of the overhang is λ , and the resulting energy per unit length, $H/(\lambda^3\delta c_0^2)$, is to be compared with the inflection energy, $K\delta c_0$. The ratio is $(H/K)(\lambda\delta c_0)^{-3} \ll 1$, since K of a lipid monolayer is a few tens $k_B T$ and $\lambda\delta c_0 \simeq 3\text{--}4$ to get an overhang (cf. Eq. (8)). Hence, the van der Waals attraction is too weak to significantly affect the overhang.

The topography of mesas and overhangs is thus a robust result which should be observable in practice. Such an observation is difficult, however, because of the small height differences and fluidity of the interface. Very recently a new experimental technique has been presented, utilizing non-specular scattering of intense light to visualize small topographic features in phospholipid monolayers [37]. Although the study was focused on features of a pure liquid-condensed phase, height differences were reported at boundaries of liquid-expanded domains coexisting with a gas phase, as well as liquid-condensed domains in a liquid-expanded phase. (Interestingly, a stronger signal was obtained in the former case, perhaps due to a larger contrast in spontaneous curvature.) It is still unclear whether these experimental findings are related to the topography discussed here or to other, more molecular effects.

Recent experiments on mixed phospholipid monolayers have revealed a new type of folding instability [21,23]. When the monolayer is compressed and enters a coexistence region, there is a critical pressure at which micron-scale folds appear. The folding is significantly more reversible than other collapse mechanisms and is therefore thought to be of key importance to the function of lungs. Figure 7 shows a pressure–area isotherm as measured for a mixed phospholipid monolayer of dipalmitoylphosphatidylcholine (DPPC) and palmitoyloleoylphosphatidylglycerol (POPG). The folding is manifested by a plateau in the isotherm. (The same phenomenon was observed in DPPG monolayers at a much higher surface tension [21].) Figure 8 presents a sequence of fluorescence microscopy images of the monolayer just before and just after the instability.

We believe that this folding phenomenon is initiated by the topographic instability of boundary regions as obtained from our model. (Further evolution and propagation of the fold are determined by other factors not taken into account in the current work, such as the viscoelasticity of the monolayer [23,38].) If the hypotheses regarding the

biological significance of the folding and its relation to topography are correct, it may represent an interesting solution of Nature to a delicate mechanical problem. Using a mixed surfactant monolayer to cover the lung leads to domain formation upon compression, which in turn allows the topographic instability and folding. Additional constituents (*e.g.*, proteins) may ensure that the folding is not preceded by other, irreversible collapse mechanisms [21]. This design provides the monolayer with a unique way to yield gracefully to compression and reduce its projected area, while avoiding irreversibility and loss of surfactant.

Folding of the mesa structure is in many cases preempted by other instabilities. One type of collapse is delamination—breakage of the monolayer into multiple layers [9,10]. It occurs when the surfactant sheet yields to a combination of bending and lateral compressive stresses. Since the mesas help relieve part of the inherent bending stresses exerted in a flat monolayer, one expects the breakage to occur (somewhat counter-intuitively) away from the boundary, inside the more frustrated domain (*i.e.*, the one having higher spontaneous curvature). Another mode of monolayer collapse is budding and ejection of vesicles into the aqueous phase [11]. Recent experiments on mixed phospholipid monolayers have shown that vesiculation is promoted by increased temperature and may coexist with folded structures [39]. The effect of topography on delamination and budding, as well as the interplay between the various collapse modes, are yet to be studied in detail.

Another general conclusion arising from this work relates to fluid surfaces of vanishing tension. Such surfactant films are encountered, *e.g.*, in emulsions, L_3 (“sponge”) phases and large, unsupported bilayer vesicles [2]. The topographic instability found for a finite tension implies that these tensionless surfaces cannot sustain a stable domain structure. To the best of our knowledge a static domain structure has never been observed in those systems. We attribute it to the inevitable shape instability that would occur near domain boundaries if such a structure existed.

We have studied a possible rippling of the domain boundary upon compression. This phenomenon arises from a competition between the topographic features accompanying the domain boundary and its bare line tension. The threshold value of line tension required to get rippling is $\tau_c \simeq g \simeq 1\text{--}10 k_B T/\text{nm}$, which is of the same order as line tension values measured in experiments [40–44]. The rippling is therefore a realistic, observable feature. There is already a well-established mechanism for shape transformations of monolayer domains, driven by a competition between line tension and long-range electrostatic interactions [45–47,40]. We offer the topographic rippling as an additional mechanism which should be observed in practice. There are three major features distinguishing the two phenomena. (i) In the electrostatic mechanism an infinite straight boundary is never stable. Consequently, the stable domain size and wavelength of boundary instability have the same scale, $L \sim q^{-1} \sim l e^{\tau/\delta p^2}$, where l is a molecular size and δp the difference in dipole densities of the two phases [45]. Hence, shape deformations occur on the scale of the entire domain [40,45,46], leading to a sequence of well-resolved, “quantized” transitions. By contrast, the length scale of the topographic rippling, $(q^*)^{-1} \sim (\delta c_0)^{-1} \lesssim 0.1 \mu\text{m}$, is much smaller than, and unrelated to, L . Thus, we expect this instability to appear as a small-scale roughening of the domain boundary. (ii) The topographic rippling, being an elastic mechanism, should not be very sensitive to changes in electrostatic parameters such as ionic strength and molecular charge. (iii) As demonstrated in Sec. V, the rippling wavelength may exhibit in certain circumstances a peculiar nonmonotonic behavior as a function of pressure. In addition, we have shown in Sec. VI that topographic rippling is inhibited near a critical point. Hence, boundary rippling could be smoothed out by heating the monolayer towards its critical temperature. This is in contrast with common surface instabilities that are usually promoted by increasing temperature.

In a recent experiment on a pure DPPC monolayer at liquid expanded–liquid condensed coexistence, a domain-boundary instability of sub-micron scale has been observed [22]. This is demonstrated in Fig. 9. At a critical pressure slight roughening appears simultaneously in all domain boundaries. Upon little further compression the roughening becomes denser and the boundaries look fuzzy due to optical limitations. A detailed presentation of this effect will be given in a forthcoming publication [22]. The small length scale of this instability (compared to the entire domain size) is in accord with the topography-induced mechanism discussed above. Yet, further study is required in order to clarify the relation between the two effects.

The phenomena described in this work—mesa formation, mesa instability, boundary rippling—arise from rather basic considerations. Nevertheless, there is still a gap between theory and experimental observations. The relation between the topographic instability as obtained from the elastic model and the observed folding in biphasic lipid monolayers is still to be established. In particular, the current theory does not account for the fully developed folded structure and its stability, as observed in experiments. Topography-induced boundary rippling and its distinction from the known electrostatic mechanism is yet another intriguing feature to be experimentally investigated. We hope to close this gap in future publications.

The mesa topography is a novel interfacial feature predicted by our work. If mesas exist, which is yet to be decisively proven by experiment, they should have important implications on various interfacial aspects, such as surface interactions with dissolved molecules, behavior in confined geometries, and possible applications for controllable nanostructures. We would like to draw special attention to the unique overhang topography predicted by the model.

Under the right compression all the domains in a biphasic monolayer should develop regular lips at their edges. Such controllable nanoscale grooves might be technologically useful, *e.g.*, for capturing and encapsulating (bio)polymers.

ACKNOWLEDGMENTS

This work was supported by the National Science Foundation under Awards Nos. DMR 9975533 and 9728858, and by its MRSEC program under Award No. 9808595. HD was partially supported by the American Lung Association (RG-085-N). CE was supported by the American Health Assistance Foundation (A1999057) and the Alzheimer's Association (IIRG-9901175). AG was supported by the Searle Scholars Program/The Chicago Community Trust (99-C-105). The experimental apparatus was made possible by an NSF CRIF/Junior Faculty Grant (CHE-9816513). KYCL is grateful for support from the March of Dimes Basil O'Connor Starter Scholar Research Award (5-FY98-0728), and the David and Lucile Packard Foundation (99-1465).

APPENDIX: DIFFERENTIAL GEOMETRY OF A RIPPLED BOUNDARY

In the rippled state we represent the domain boundary by the curve $\mathbf{R}(y) = (x = a \sin qy, y, z = 0)$ and parameterize the monolayer surface as

$$\begin{aligned} \mathbf{r}(s, t) &= (x(s, t), y(s, t), z(s, t)) \\ x(s, t) &= \int_0^s \cos \theta(s') ds' + a \sin qt, \quad y(s, t) = t, \quad z(s, t) = \int_0^s \sin \theta(s') ds'. \end{aligned} \quad (\text{A1})$$

We now need to represent the various properties of the surface using the “material coordinates” (s, t) [48].

The determinant of the metric tensor associated with the surface of Eq. (A1) is

$$\Gamma = (\partial_s \mathbf{r} \times \partial_t \mathbf{r})^2 = 1 + (qa \cos qt \sin \theta)^2. \quad (\text{A2})$$

The Jacobian of the transformation $(x, y) \rightarrow (s, t)$ is $J = \partial_s x \partial_t y - \partial_t x \partial_s y = \cos \theta$. Using these expressions we find the area element,

$$dA(s, t) = \Gamma^{1/2} ds dt = (1 + q^2 a^2 \cos^2 qt \sin^2 \theta)^{1/2} ds dt, \quad (\text{A3})$$

and its projection onto the xy plane,

$$dA_p(s, t) = J ds dt = \cos \theta ds dt. \quad (\text{A4})$$

An element of the boundary curve is given by $d\mathbf{R} = (qa \cos qt, 1, 0) dt$, and the resulting arc-length element is

$$dR(s, t) = [1 + (qa \cos qt)^2]^{1/2} dt. \quad (\text{A5})$$

What is left to calculate is the local surface curvature, $c(s, t)$. The local normal to the surface is given by

$$\mathbf{n} = \Gamma^{-1/2} (\partial_s \mathbf{r} \times \partial_t \mathbf{r}) = \Gamma^{-1/2} (-\sin \theta, qa \cos qt \sin \theta, \cos \theta).$$

The mean curvature can then be calculated either from the trace of the curvature tensor,

$$c(s, t) = -\frac{1}{2} \text{tr}(\partial n_i / \partial r_j),$$

or by momentarily resorting to the Monge representation,

$$c = \nabla \cdot [\Gamma^{-1/2} \nabla z(x, y)],$$

where the ∇ operator is defined in the xy plane. The result is

$$c(s, t) = \Gamma^{-3/2} [(1 + q^2 a^2 \cos^2 qt) \dot{\theta} + q^2 a \sin qt \sin \theta]. \quad (\text{A6})$$

- [1] *Micelles, Membranes, Microemulsions, and Monolayers*, edited by W. M. Gelbart, A. Ben-Shaul and D. Roux (Springer-Verlag, New York, 1989).
- [2] S. A. Safran, *Statistical Thermodynamics of Surfaces, Interfaces, and Membranes* (Addison-Wesley, New York, 1994).
- [3] K. S. Birdi, *Lipid and Biopolymer Monolayers at Liquid Interfaces* (Plenum Press, New York, 1989). K. S. Birdi, *Self-Assembly Monolayer Structures of Lipids and Macromolecules at Interfaces* (Kluwer Academic/Plenum Publishers, New York, 1999).
- [4] B. Robertson and H. L. Halliday, *Biochim. Biophys. Acta* **1408**, 346 (1998).
- [5] G. D. Guttman and D. Andelman, *J. Phys. II France* **3**, 1411 (1993).
- [6] S. T. Milner, J.-F. Joanny and P. Pincus, *Europhys. Lett.* **9**, 495 (1989).
- [7] A. Saint-Jalmes, F. Graner, F. Gallet and B. Houchmandzadeh, *Europhys. Lett.* **28**, 565 (1994).
- [8] J.-G. Hu and R. Granek, *J. Phys. II France* **6**, 999 (1996).
- [9] H. E. Ries and H. Swift, *Langmuir* **3**, 853 (1987).
- [10] E. Hatta, H. Hosoi, H. Akiyama, T. Ishii and K. Mukasa, *Eur. Phys. J. B* **2**, 347 (1998).
- [11] P. Tchoreloff, A. Gulik, B. Denizot, J. E. Proust and F. Puisieux, *Chem. Phys. Lipids* **59**, 151 (1991).
- [12] D. Andelman, F. Brochard, P.-G. de Gennes and J.-F. Joanny, *C.R. Acad. Sci. Paris Ser. C* **301**, 675 (1985). D. Andelman D., Brochard F. and J.-F. Joanny, *J. Chem. Phys.* **86**, 3673 (1987). D. Andelman, F. Brochard and J.-F. Joanny, *Proc. Natl. Acad. Sci. USA* **84**, 4717 (1987).
- [13] M. Seul and D. Andelman, *Science* **267**, 476 (1995).
- [14] S. Leibler and D. Andelman, *J. Phys. France* **48**, 2013 (1987).
- [15] D. Andelman D., T. Kawakatsu and K. Kawasaki, *Europhys. Lett.* **19**, 57 (1992). T. Kawakatsu, D. Andelman, K. Kawasaki and T. Taniguchi, *J. Phys. II France* **3**, 971 (1993). T. Taniguchi, K. Kawasaki, D. Andelman and T. Kawakatsu, *J. Phys. II France* **4**, 1333 (1994).
- [16] Z. G. Wang, *J. Chem. Phys.* **99**, 4191 (1993).
- [17] F. C. MacKintosh and S. A. Safran, *Phys. Rev. E* **47**, 1180 (1993).
- [18] H. Kodama and S. Komura, *J. Phys. II France* **3**, 1305 (1993).
- [19] J. L. Harden and F. C. MacKintosh, *Europhys. Lett.* **28**, 495 (1994).
- [20] F. Jülicher and R. Lipowsky, *Phys. Rev. E* **53**, 2670 (1996). P. B. Sunil Kumar and M. Rao, *Phys. Rev. Lett.* **80**, 2489 (1998). W. T. Gózdź and G. Gompper, *Phys. Rev. E* **59**, 4305 (1999). P. B. Sunil Kumar, G. Gompper and R. Lipowsky, *Phys. Rev. E* **60**, 4610 (1999).
- [21] M. M. Lipp, K. Y. C. Lee, J. A. Zasadzinski and A. J. Waring, *Science* **273**, 1196 (1996). M. M. Lipp, K. Y. C. Lee, A. Waring and J. A. Zasadzinski, *Biophys. J.* **72**, 2783 (1997). M. M. Lipp, K. Y. C. Lee, D. Y. Takamoto, J. A. Zasadzinski and A. J. Waring, *Phys. Rev. Lett.* **81**, 1650 (1998).
- [22] C. Ege and K. Y. C. Lee, unpublished.
- [23] H. Diamant, T. A. Witten, A. Gopal and K. Y. C. Lee, *Europhys. Lett.* **52**, 171 (2000).
- [24] One can just as well consider also differing bending moduli of the two domains [23]. The resulting expressions are more cumbersome with essentially the same physics. For brevity we consider in the current paper a single, uniform bending modulus K .
- [25] The exact relation between the applied lateral pressure and surface tension in a nonflat monolayer is a subtle issue [8]. In this paper we bypass it by referring to the tension γ alone, bearing in mind that it must decrease upon increasing pressure.
- [26] We do not consider fluctuations of the surface; its equilibrium shape is thus given by the minimum of the elastic energy. This “zero-temperature” assumption is well justified in the current case, as will be demonstrated in Sec. VII.
- [27] We ignore in this paper the possibility of a sharp change in slope, a crease, at the contact line. Such a crease would alter some of our quantitative conclusions. Though such creases are consistent with the symmetry of the system, we know of no estimate of their magnitude.
- [28] All of the above results, except for the precise profile (Eq. (7)), hold also for a finite sheet clamped at its ends (*i.e.*, maintaining the boundary conditions of vanishing θ and $\dot{\theta}$ at both ends).
- [29] Here the bare line tension τ is assumed to contain all the energetic contributions proportional to the boundary length, including both short-range and electrostatic interactions; see also Ref. [45].
- [30] Note again that the relevance of this instability relies on the nonlinearity of our calculation. In a linearized theory (assuming $\theta_0 \ll 1$) one would get for the reduction in line tension $g \simeq (-\theta_0/2)K\delta c_0$, which could not compete with the bare line tension τ .
- [31] L. D. Landau and E. M. Lifshitz, *Theory of Elasticity* (Butterworth-Heinemann, Oxford, 1986), Chap. II.
- [32] J. J. Binney, N. J. Dorwick, A. J. Fisher and M. E. J. Newman, *The Theory of Critical Phenomena* (Oxford University Press, Oxford, 1993).
- [33] M. E. Fisher, *Phys. Rev.* **176**, 257 (1968).
- [34] L. Onsager, *Phys. Rev.* **65**, 117 (1944).
- [35] B. Widom, *J. Chem. Phys.* **43**, 3892 (1965).
- [36] J. N. Israelachvili, *Intermolecular & Surface Forces* (Academic Press, London, 1991), Chap. 11.
- [37] W. R. Schief, L. Touryan, S. B. Hall and V. Vogel, *J. Phys. Chem B* **104**, 7388 (2000). W. R. Schief, S. B. Hall and V. Vogel, *Phys. Rev. E* **62**, 6831 (2000).

- [38] R. Miller, R. Wüstneck, J. Krägel and G. Kretzschmar, *Colloid Surf. A* **111**, 75 (1996).
 [39] A. Gopal and K. Y. C. Lee, unpublished.
 [40] K. J. Stine and C. M. Knobler, *Phys. Rev. Lett.* **65**, 1004 (1990).
 [41] P. Muller and F. Gallet, *Phys. Rev. Lett.* **67**, 1106 (1991).
 [42] D. J. Benvegnu and H. M. McConnell, *J. Phys. Chem.* **96**, 6820 (1992).
 [43] S. Rivière, S. Hénon, J. Meunier, G. Albrecht, M. M. Boissonnade and A. Baszkin, *Phys. Rev. Lett.* **75**, 2506 (1995).
 [44] S. Wurlitzer, P. Steffen and T. M. Fischer, *J. Chem. Phys.* **112**, 5915 (2000).
 [45] D. J. Keller, J. P. Korb and H. M. McConnell, *J. Phys. Chem.* **91**, 6417 (1987). H. M. McConnell and V. T. Moy, *J. Phys. Chem.* **92**, 4520 (1988). H. M. McConnell, *J. Phys. Chem.* **94**, 4728 (1990). H. M. McConnell, *J. Phys. Chem.* **96**, 3167 (1992). K. Y. C. Lee and H. M. McConnell, *J. Phys. Chem.* **97**, 9532 (1993).
 [46] M. Seul and J. Sammon, *Phys. Rev. Lett.* **64**, 1903 (1990). M. Seul, *J. Phys. Chem.* **97**, 2941 (1993).
 [47] R. E. Goldstein and D. P. Jackson, *J. Phys. Chem.* **98**, 9626 (1994).
 [48] See, *e.g.*, Ref. [2], Chap. 1.

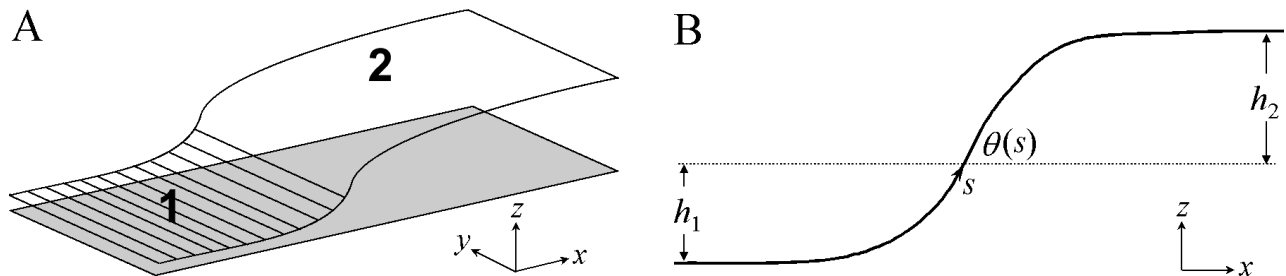


FIG. 1. A) Schematic sketch of the monolayer in the boundary region. A boundary lying parallel to the y axis separates two large domains denoted by 1 and 2. B) Cross-section parallel to the xz plane. The monolayer conformation is parameterized by the angle $\theta(s)$ it makes with the xy reference plane at curvilinear distance s from the boundary.

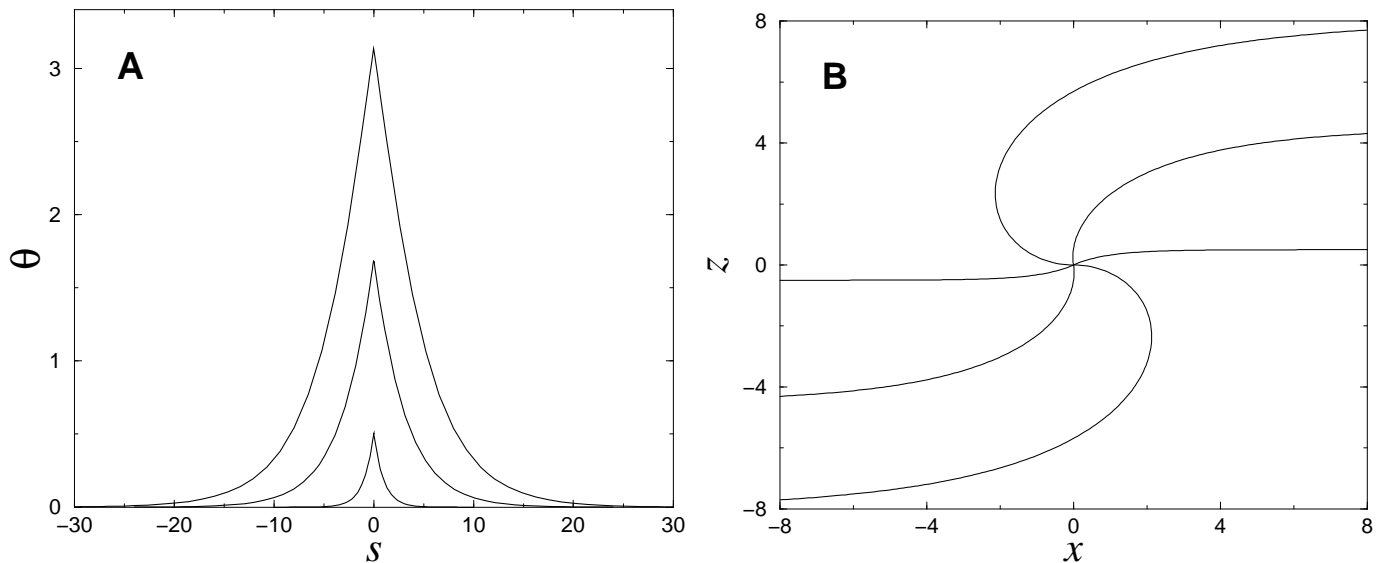


FIG. 2. A) Slope angle profiles near a sharp domain boundary as compression is increased. The curves are obtained from Eqs. (7) and (8) using the values (from bottom to top) $\lambda\delta c_0 = 1, 3, 4$. B) The corresponding spatial conformations. All lengths are given in units of $(\delta c_0)^{-1}$.

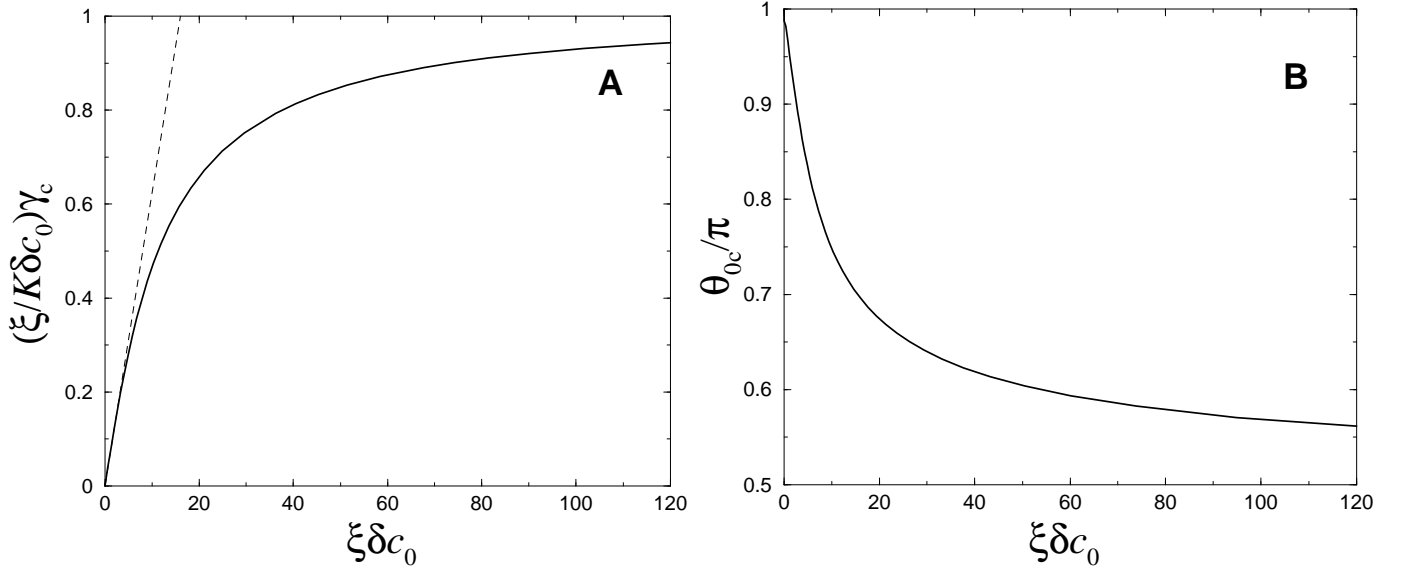


FIG. 3. Effect of diffuse boundary on mesa instability. A) Rescaled critical tension, $(\xi/K\delta c_0)\gamma_c$, required for the transition. The solid line is the result for a boundary of finite thickness (*i.e.*, the scaling function $F(x)$ of Eq. (23)). The dashed line is the corresponding result for an infinitely sharp boundary (Eq. (12)). B) Critical inflection angle. For very sharp boundaries the angle at instability is π , whereas for very diffuse ones it is reduced to $\pi/2$.

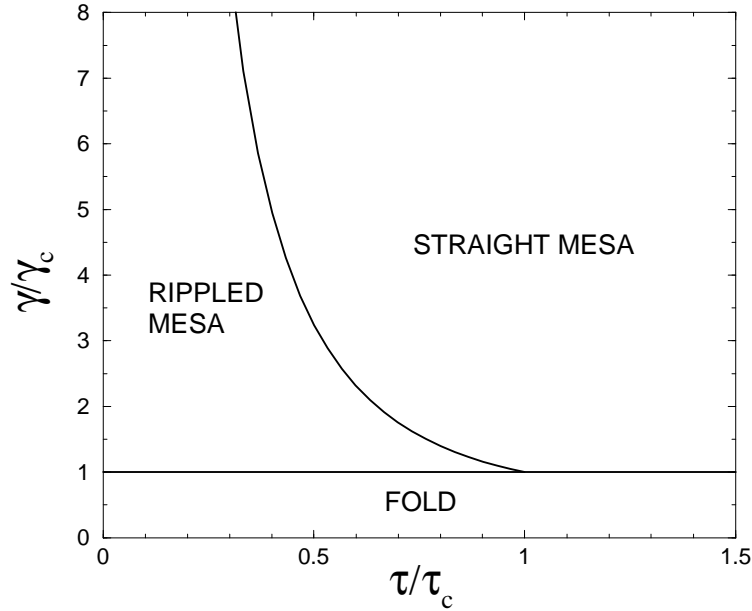


FIG. 4. Surface tension–line tension diagram of topographies for a sharp domain boundary. If $\tau > \tau_c = (\pi - 2)K\delta c_0$ the mesa topography remains straight upon decreasing surface tension until it becomes unstable at $\gamma = \gamma_c = \frac{1}{16}K(\delta c_0)^2$. If $\tau < \tau_c$ the mesa wall ripples below a surface tension $\gamma = \gamma_r > \gamma_c$.

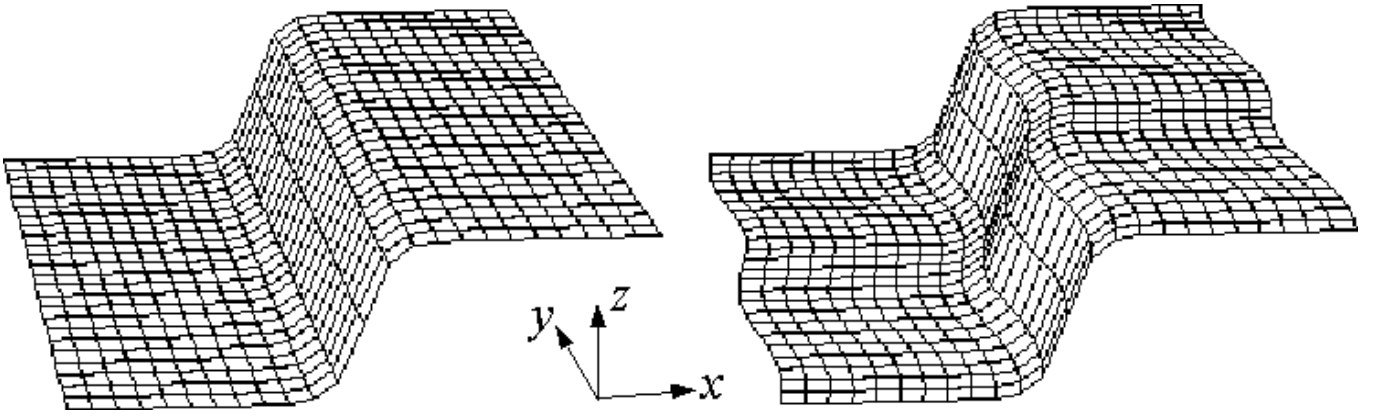


FIG. 5. Schematic sketch of the assumed rippling perturbation.

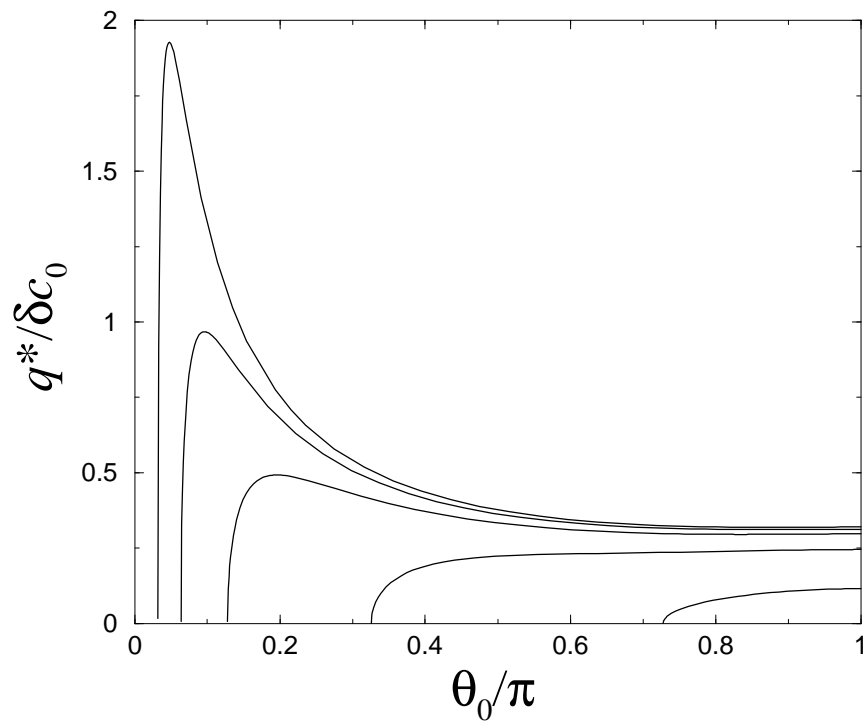


FIG. 6. Dependence of rippling wavenumber on inflection angle for various values of line tension (from top to bottom): $\tau/(K\delta c_0) = 0.05, 0.1, 0.2, 0.5, 1$. For higher line tension, $\tau/(K\delta c_0) > \pi - 2 \simeq 1.14$, there is no rippling.

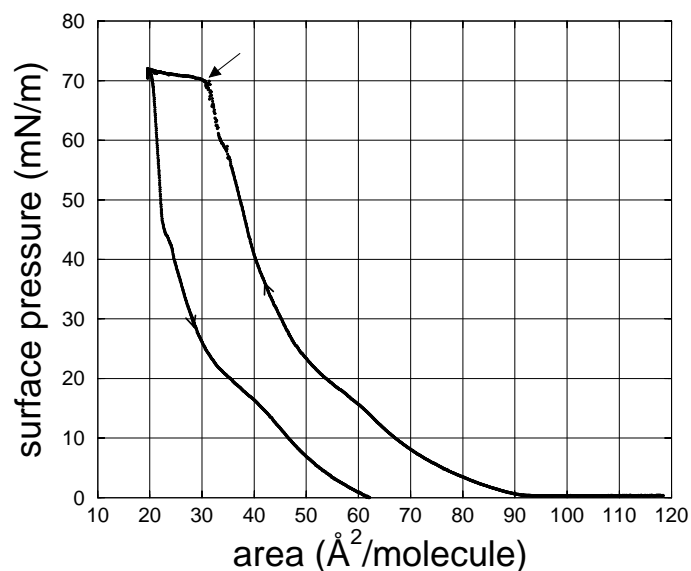


FIG. 7. Pressure–area isotherm for a mixed monolayer of DPPC and POPG, as measured during a compression/expansion cycle in a Langmuir trough. The mole ratio is DPPC:POPG=7:3 and the temperature 25°C. The folding instability is indicated by an arrow.

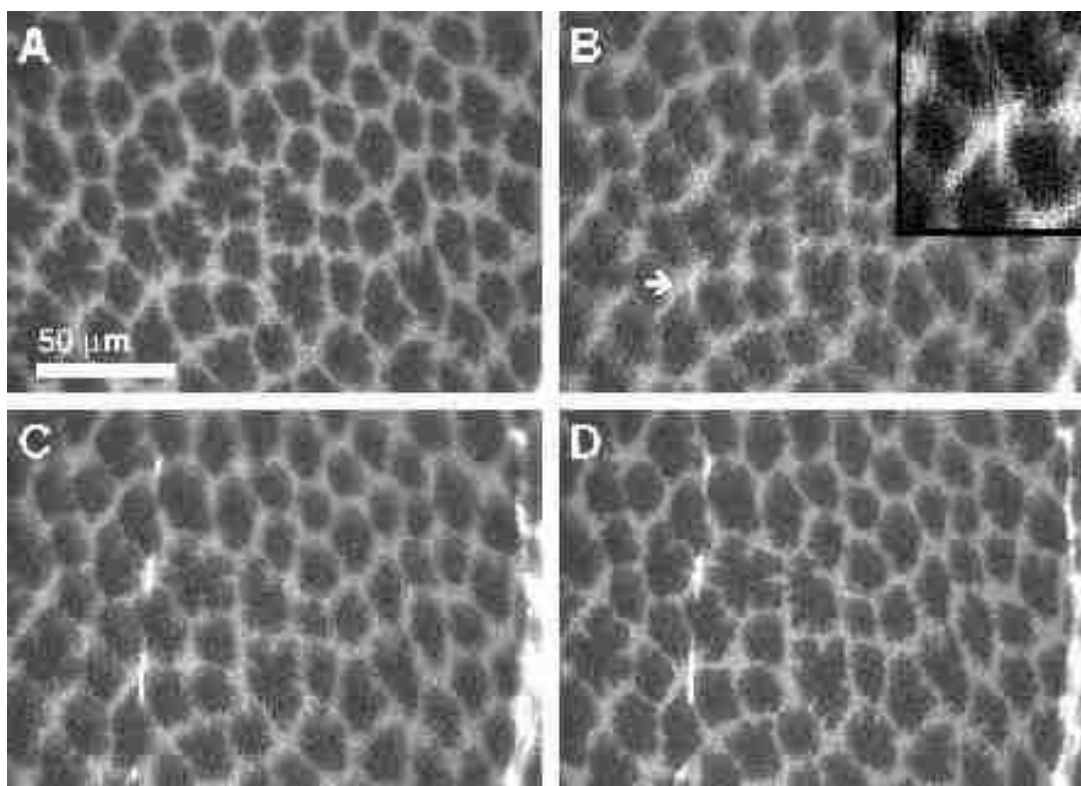


FIG. 8. Fluorescence microscopy images of the folding instability. A) Section of the monolayer just before folding ($t = 0$), exhibiting the biphasic domain structure. Dark regions are DPPC-rich; bright ones are POPG-rich. B) The same section at $t = 1/30$ s. A micron-scale fold appears in between domain walls (indicated by arrow). The image is blurred because of monolayer movement during folding. The inset shows a contrast-enhanced image of the fold, magnified by 50 percent. C) The fold at $t = 2/30$ s, having propagated to nearby domains. D) The fold at $t = 4/30$ s, after the fast monolayer movement has ceased.

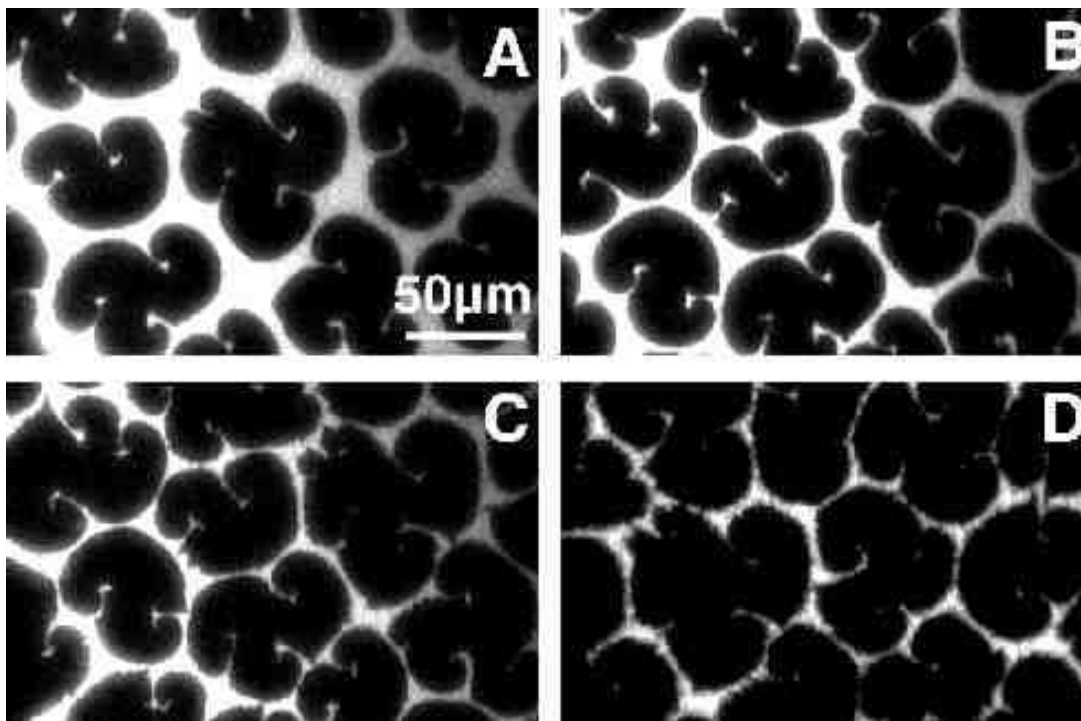


FIG. 9. Roughening of domain boundaries upon compression, as observed by fluorescence microscopy. The monolayer consists of DPPC phospholipids and lies over an aqueous solution of 0.2M NaCl at temperature 24.5°C. Dark regions correspond to a liquid-condensed phase and bright ones to a liquid-expanded phase. The lateral pressures and molecular areas (in mN/m and \AA^2 , respectively) are: A) 16.9, 54.8; B) 19.4, 53.0; C) 21.6, 51.9; D) 23.4, 51.2. Images were contrast-enhanced.